Dynamics of Atmospheres and Oceans 115 (2026) 101691

Contents lists available at ScienceDirect

Dynamics of Atmospheres and Oceans

journal homepage: www.elsevier.com/locate/dynatmoce

# A combined modeling and EOF approach to characterize the hydrodynamics of a semi-enclosed bay

Diego Bindoni [a,b,*], Jacopo Alessandri [c], Ivan Federico [c], Antonella Abbà [a]

[a] Department of Aerospace Science and Technology, Politecnico di Milano, Via La Masa, 34, Milano, 20156, Italy
[b] Department of Electronics, Information and Bioengineering, Politecnico di Milano, Via Ponzio 34/5, Milano, 20133, Italy
[c] CMCC Foundation – Euro-Mediterranean Center on Climate Change, Italy

ARTICLE INFO

*Keywords:*
EOF
Semi-enclosed bay
Augusta bay

ABSTRACT

Semi-enclosed coastal basins are highly vulnerable ecosystems where anthropogenic pressures are often amplified by intricate, topologically-constrained hydrodynamics that lead to low water renewal and pollutant trapping. Understanding their circulation drivers is therefore critical for effective environmental management. In this study, we investigate a representative semi-enclosed basin by combining a high-resolution, three-dimensional numerical model with Empirical Orthogonal Function (EOF) analysis to deconstruct and interpret the system's circulation. The results show that EOF analysis effectively isolates the system's primary drivers. The leading modes of surface circulation are unequivocally linked to wind forcing, revealing a clear seasonal modulation of wind-driven currents. The analysis of vertical density structures and interannual analysis demonstrate that seasonal stratification and open sea currents are the dominant controls on water exchange; strong summer stratification inhibits renewal, whereas winter mixing promotes vigorous baroclinic circulation. Higher-order modes of the vertical density transects successfully identify exchange patterns at the openings, revealing that a portion of the system's variance is also explained by the presence and dynamics of the pycnocline, which modulates internal mixing and recirculation. This work highlights the intricate balance between external forcing (wind), internal dynamics (stratification), basin geometry and external currents in shaping circulation. It validates the combined use of high-resolution modeling and EOF analysis as a powerful approach to provide a clear and quantitative framework for identifying the key physical processes governing the hydrodynamics of semi-enclosed coastal systems.

## 1. Introduction

Semi-enclosed coastal basins represent some of the most complex and vulnerable environments within the marine domain. Their circulation patterns are typically governed by a delicate interplay between local forcings, such as wind, tides, and exchanges with the adjacent open sea. Understanding the hydrodynamic behavior of these systems is essential for assessing their ecological status, their capacity to dilute and transport pollutants, and their resilience to both anthropogenic stressors and climate variability. Despite this relevance, many such basins remain poorly characterized, with high-resolution, long-term numerical modeling representing a useful tool to fill these knowledge gaps.

The Bay of Augusta, located along the eastern coast of Sicily in the central Mediterranean Sea, exemplifies such a semi-enclosed system. It is an embayment of approximately 23.5 km$^2$, partially isolated from the Ionian Sea by a series of artificial dams and

* Corresponding author.
*E-mail address:* diego.bindoni@polimi.it (D. Bindoni).

https://doi.org/10.1016/j.dynatmoce.2026.101691
Received 31 December 2025; Received in revised form 15 June 2026; Accepted 29 June 2026
Available online 3 July 2026

breakwaters constructed in the mid-20th century. The bay has historically been affected by intense industrial activity, which has led to severe environmental degradation (Ausili et al., 2020) and its designation as a Site of National Interest (SIN) by the Italian Ministry for the Environment (Law 426/98, DM 10 January 2010). Consequently, it has become the subject of extensive monitoring and remediation efforts (Salvagio Manta et al., 2016; Benedetti et al., 2022; Romano et al., 2021; Sprovieri et al., 2022). Nevertheless, the circulation within the bay, shaped by both natural dynamics and anthropogenic modifications, remains insufficiently investigated at the spatial and temporal scales required for robust environmental assessment and management.

Previous studies have offered only partial insights into the hydrodynamics of Augusta Bay. For example, Raffa and Hopkins (2004) conducted a five-day field campaign in October 2001, performing measurements along transects outside the bay. While informative, this experiment could not capture seasonal or interannual variability, nor the internal circulation processes that may govern tracer retention, pollutant dispersion, and water exchanges through the breakwaters. Early modeling efforts have provided a preliminary baseline of hydrodynamic characterization. Lisi et al. (2009) applied a two-dimensional depth-averaged (2DH) hydrodynamic model, coupled with a Lagrangian dispersion scheme, to evaluate water renewal efficiency. It should be noted that the Bay of Augusta lacks significant riverine discharge; consequently, the internal density structure is primarily governed by air-sea heat exchange and the intrusion of open-sea water masses through the breakwater openings, rather than localized freshwater buoyancy fluxes.

Subsequently, Marchis et al. (2014) extended the analysis using, for the first time, a fully three-dimensional numerical model. The model successfully reproduced the main hydrodynamic features, capturing both the flow configuration and current intensities. Their results also highlighted the differentiated role of external forcings: tides emerged as the primary mechanism driving mass exchange between the port and the open sea, whereas wind forcing was shown to modulate the internal circulation. Beyond the bay, circulation patterns in the adjacent Ionian Sea have also been investigated. For instance, Ciappa (2009) analyzed surface circulation in the Sicily Channel and Ionian Sea using MODIS chlorophyll-a imagery collected between 2003 and 2007. This regional perspective provides useful context for understanding external influences on the circulation of Augusta Bay, which are not explicitly addressed in previous studies focused solely on the inner basin.

Building on this background, the present study provides a high-resolution, four-year-long hydrodynamic simulation of the inner Bay of Augusta. Unlike previous modeling efforts, this work employs a refined unstructured grid (down to $\approx 40$ m resolution) to resolve accurately small-scale circulation features and interaction with topography. More importantly, this work advances beyond the foundational baseline established by Marchis et al. (2014) by replacing short-term qualitative characterizations with a comprehensive multi-year analysis capable of identifying inter-seasonal and inter-annual shifts in circulation regimes. Furthermore, by mapping the domain over an extended four-year window, this framework explicitly isolates and quantifies the remote influence of offshore Ionian currents on the inner basin's mass exchange, uncovering a multi-scale mechanism that remains unaddressed in local-scale coastal models. The main objectives are to characterize the inter-seasonal and inter-annual circulation features, investigate exchange dynamics with the open sea, and assess the bay's interseasonal variability in terms of temperature, salinity and currents. By incorporating wind and physical boundary data into a numerical ocean model, we aim to resolve both dominant seasonal signals and shorter-term variability that may control residence times, mixing processes, and pollutant transport.

In addition to the modeling framework, this study applies Empirical Orthogonal Function (EOF) analysis as a diagnostic tool to extract coherent modes of variability from the simulated fields. EOF analysis has been successfully employed in various oceanographic contexts (Elken et al., 2011; Morales-Marín et al., 2017; Ren et al., 2020; Tolkova and Power, 2011; Causio et al., 2024) to identify spatially and temporally persistent patterns in current and temperature data. For Augusta Bay, where multiple forcings interact within a confined domain, the major methodological novelty lies in utilizing the EOF decomposition not merely for data reduction, but as a formal diagnostic tool to mathematically disentangle and quantify overlapping drivers. This approach allows us to separate local atmospheric momentum inputs from broader density-driven patterns, establishing clear, quantitative linkages to identify dominant circulation structures of horizontal currents and vertical mixing processes. By evaluating these processes over a four-year window, the study provides a robust assessment of interannual shifts in circulation regimes that shorter field campaigns or seasonal models cannot capture. This approach offers both a physical interpretation of the modeled dynamics and a reduced-order framework that can inform future monitoring and predictive efforts.

The results presented here represent a foundational contribution to the scientific understanding of Augusta Bay and, more broadly, to the study of semi-enclosed basins in the Mediterranean and beyond. Specifically, the characterization of interannual variability and the quantification of hydrodynamic drivers offer a more precise framework for predicting the long-term transport and fate of industrial pollutants within the SIN area. Moreover, the combined application of high-resolution modeling and EOF analysis demonstrates a transferable methodology for investigating similar environments where observational data remain scarce but where evidence-based environmental management is urgently required.

The paper is structured as follows. The first part is dedicated to the methodology, providing a brief overview of the model, a description of the computational setup, and a short discussion of the Empirical Orthogonal Function (EOF) technique and statistical tools employed. The results section then presents the validation of the simulated dataset against satellite measurements and in situ temperature and salinity profiles, followed by an analysis in terms of seasonal averages, vertical transects and adoption of EOF for pattern and driver's identification. An interannual analysis is also assessed to reinforce the discussion. Finally, the paper concludes with a summary of the main findings.

## 2. Methodology

To investigate the hydrodynamic behavior of the Bay of Augusta, we set up a high-resolution numerical simulation using the parallel version of SHYFEM-MPI (System of Hydrodynamic Finite Element Modeling) framework (Micaletto et al., 2022). SHYFEM-MPI is a three-dimensional, free-surface shallow-water hydrodynamic model designed to simulate estuarine and coastal marine

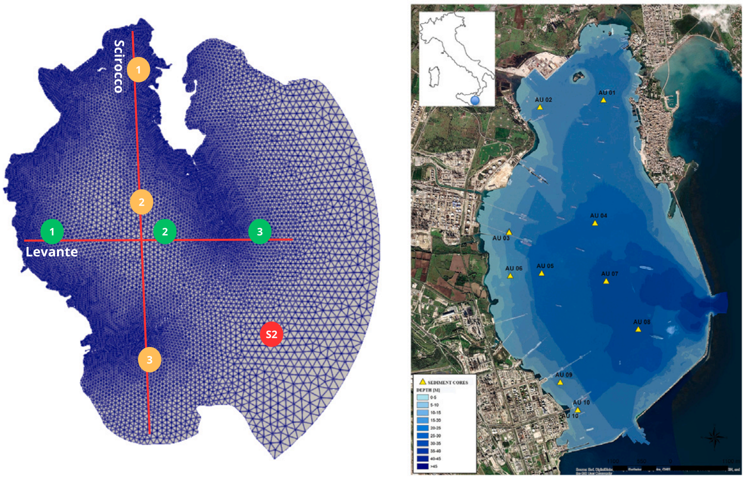


**Fig. 1.** On the left, unstructured mesh generated for the bay of Augusta, including a small portion of open sea. On the right, the inner bay bathymetry from Romano et al. (2021) that has been digitalized for the present computational grid. Red lines represent the two transects (named Levante and Scirocco) defined for the analysis in Section 3.5. Colored numbers are referred to N2 profiles points location, used in Fig. 11. The red "S2" dot identifies the location of the probe used for validation in Section 3.1.

environments. It solves the primitive equations of fluid motion under the hydrostatic and Boussinesq approximations using an unstructured finite element horizontal grid and zeta layer vertical coordinates. This flexible mesh configuration is particularly well-suited for representing complex coastlines, shallow bathymetry, and narrow inlets, making it ideal for semi-enclosed and morphologically intricate domains such as Augusta Bay. SHYFEM-MPI accounts for barotropic, baroclinic, and atmospheric pressure gradients as well as wind drag and bottom friction, non-linear advection, and vertical turbulent processes. The set of equations at the core of the SHYFEM-MPI model and their numerical solution can be consulted at Verri et al. (2023) and Umgiesser et al. (2004).

### 2.1. Model configuration

The computational domain covers the entire inner Bay of Augusta and extends beyond its artificial barriers to allow adequate exchange with the adjacent Ionian Sea (Fig. 1, left). The unstructured horizontal grid includes an higher spatial resolution within the bay and a coarser resolution in the outer boundary zone, spanning from 40 m to 1 km close to the boundary. In Fig. 1 (right), a map showing the bathymetry of the inner bay measured during the experimental campaign in Romano et al. (2021) is showed, since it has been digitalized and employed in the present set-up. Vertically, the water column is discretized into 40 vertical layers, spanning from 1.5 m, set as a minimum depth for the model, to 120 m. In order to correctly represent the inner bay dynamics, the layer thickness has been varied along the vertical column, in order to have 26 layers in the first 40 m of depth and 17 in the first 20 m.

The simulation spans a continuous four-year period, starting from December 2021 until November 2025, and is driven by both atmospheric and oceanographic boundary conditions. The model timestep can vary to ensure numerical stability by keeping the Courant number lower than 1 and maintaining a marching time step between 50 and 90 s. No wave module has been coupled to the model, following the results obtained from Lisi et al. (2009), whose simulations indicated that short waves do not induce significant circulation within the port, as wave propagation is strongly damped by the three breakwaters. Atmospheric surface forcing was derived from the ECMWF IFS010 dataset (European Centre for Medium-Range Weather Forecasts, 2025), available at 6-hour temporal resolution and 1/10° spatial resolution. The dataset includes surface wind stress, air temperature, relative humidity, surface pressure, and net heat fluxes. These parameters were interpolated onto the SHYFEM-MPI grid and applied as surface boundary conditions, providing realistic and temporally resolved meteorological forcing throughout the simulation period. Temporal consistency between the wind forcing and the remaining oceanographic fields was maintained through linear interpolation across the respective sampling intervals. Open boundary conditions at the offshore extent of the domain were prescribed using data from the Copernicus Marine Environment Monitoring Service (CMEMS) Global Ocean Physics Analysis and Forecast product, accessed via the Copernicus Marine DataStore (E.U. Copernicus Marine Service Information (CMEMS), 2025). This dataset provides hourly data for sea level, temperature, salinity, and three-dimensional current velocities with a spatial resolution of 1/24°. The extracted boundary values were spatially and vertically interpolated onto the SHYFEM-MPI mesh to ensure consistency with the internal model structure. The high temporal resolution (1 h) allowed for accurate representation of tidal components. Initial fields for temperature and salinity were obtained from the CMEMS dataset at the start of the simulation. A one-month spin-up period was performed to reduce initialization transients and allow adjustment to boundary and surface forcing. The turbulence closure model is the GOTM (General Ocean Turbulence Model) (Burchard and Bolding, 2001). Bottom stress was applied using a quadratic drag law (Drag coefficient = 0.0025), and the bathymetric data were compiled from nautical charts taken from Romano et al. (2021)

(Fig. 1, right) for the inner bay and EMODnet Bathymetry portal (EMODnet Bathymetry Consortium, 2024) for the outside bay area close to the shelf. A more detailed description of the input parameters and the formalization of physical processes can be found in Appendix. Model outputs were saved at hourly intervals and subsequently post-processed to extract inter-seasonal and inter-annual patterns.

To conclude, in the study, we adopted the conventional methodology in ocean season definition:

- Winter: December, January, February (W);
- Spring: March, April, May (SP);
- Summer: June, July, August (SU);
- Autumn: September, October, November (A).

### 2.2. Empirical Orthogonal Function

An Empirical Orthogonal Function (EOF) analysis was applied to the simulated velocity field and to identify dominant spatial modes of variability and their temporal evolution. EOF analysis is a statistical technique used to extract dominant patterns of variability from spatiotemporal data (Zhang and Moore, 2015). Given a velocity field $\mathbf{u}(\mathbf{x}, t)$, anomalies are first constructed by removing the temporal mean:

$$\mathbf{u}'(\mathbf{x}, t) = \mathbf{u}(\mathbf{x}, t) - \overline{\mathbf{u}(\mathbf{x})}.$$

The covariance matrix is then defined as

$$C = \frac{1}{N}\mathbf{U}'\mathbf{U}'^{\top},$$

where $\mathbf{U}'$ is the anomaly matrix with columns representing time snapshots and $N$ the number of samples. The EOFs are obtained as the eigenvectors $\mathbf{e}_k$ of $C$:

$$C\mathbf{e}_k = \lambda_k \mathbf{e}_k,$$

with $\lambda_k$ denoting the variance explained by the $k$th mode. The temporal evolution of each mode is given by the principal component (PC),

$$a_k(t) = \mathbf{e}_k^{\top}\mathbf{u}'(t).$$

This decomposition reduces hydrodynamic structures into orthogonal spatial patterns and their associated time series, allowing the attribution of variability to physical forcing mechanisms and the identification of persistent circulation features. In the present project, spatial structures will be plotted, while the associated temporal time series, that modulate the EOF structures, will be employed to perform statistical analyses.

### 2.3. Statistical analysis and performance metrics

The relationship between the EOF structures and external forcing mechanisms was evaluated using a suite of diagnostic statistical tools. The linear association between wind stress and current velocity components was quantified primarily through the Pearson correlation coefficient ($r$) (Pearson, 1895). To ensure the integrity of these statistical inferences, $p$-values were calculated for all coefficients to assess significance against the null hypothesis. To ensure the statistical significance of the correlations between atmospheric forcing and the reconstructed EOF modes, the effective degrees of freedom ($N_{eff}$) were estimated. Given that hydrodynamic time series often exhibit high temporal autocorrelation, treating each hourly sample as an independent observation can lead to an overestimation of statistic and an artificially low $p$-value. To account for this, $N_{eff}$ was calculated following the methodology proposed by Pyper and Peterman (1998):

$$N_{eff} \approx N\frac{1 - r_1 r_2}{1 + r_1 r_2} \tag{1}$$

where $N$ is the total number of samples, and $r_1, r_2$ are the lag-1 autocorrelation coefficients for the wind stress and current velocity series, respectively. This adjusted $N_{eff}$ was subsequently used to determine the significance levels ($p$-values) for all reported Pearson correlations. By utilizing this conservative approach, we ensure that the identified relationships represent robust physical couplings rather than statistical artifacts of the high-frequency sampling.

To provide a comprehensive assessment of the model's predictive skill and systematic behavior, several performance metrics were utilized. The Mean Error (ME) was calculated to identify systematic bias, representing the average difference between the $N$ model-predicted values ($\hat{y}_i$) and the observed or satellite-derived datasets ($y_i$), defined as $ME = \frac{1}{N}\sum_{i=1}^{N}(y_i - \hat{y}_i)$. This was complemented by the Root Mean Square Error, $RMSE = \sqrt{\frac{1}{N}\sum_{i=1}^{N}(y_i - \hat{y}_i)^2}$, which provides a measure of the average magnitude of prediction errors while placing a higher penalty on larger deviations. To offer a more holistic evaluation than that provided by standard correlation alone, the Kling–Gupta Efficiency (KGE) coefficient was employed. The KGE integrates three distinct components like Pearson correlation ($r$), standard deviation ratio ($\alpha$), and bias ratio ($\beta$) into a single metric, defined as $KGE = 1 - \sqrt{(r-1)^2 + (\alpha-1)^2 + (\beta-1)^2}$, where a value of 1 indicates a perfect match between the simulation and observations. Finally, the fraction of variance in the temporal EOF modes explained by predictors such as wind stress was determined via the coefficient of determination ($R^2$) derived from simple linear regression models.

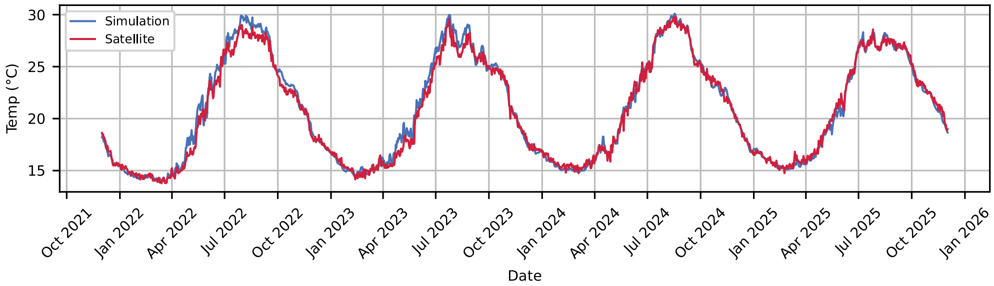


**Fig. 2.** Time series of simulated against satellite foundation temperature over the 4 years under analysis.

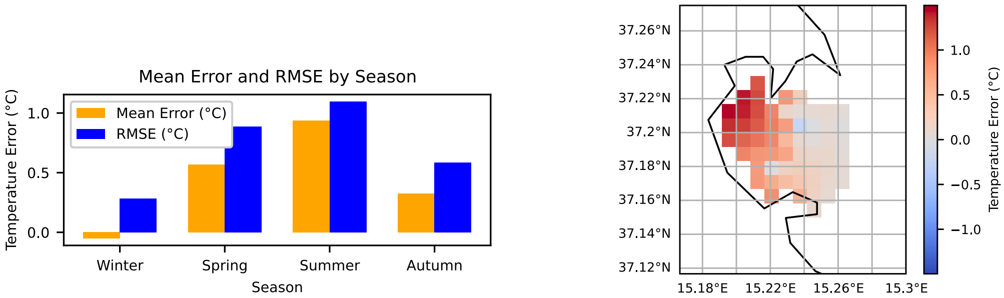


(a) (b)

**Fig. 3.** Comparison plots between simulated and satellite datasets. (a) represents an histogram of ME and RMSE for each season, averaged over the two simulated years. (b) represents the area ME distribution averaged over the 4 summer periods.

## 3. Results

### 3.1. Model validation

The predictive performance of the SHYFEM-MPI model was assessed through a dual-platform validation strategy. First, spatial consistency was evaluated using L4 satellite-derived Sea Surface Temperature (SST) (Buongiorno Nardelli et al., 2013; Copernicus Marine Service, 2025; Fanelli et al., 2024). Second, the vertical thermohaline structure was validated against an in situ dataset provided by the Agenzia Regionale per la Protezione dell'Ambiente (ARPA) (Fig. 4). The ARPA measurement campaign utilized an IDRONAUT

(OCEAN SEVEN 316/316Plus) multiparametric probe, conducting bimestral sampling over the period from April 2024 to August 2025. The monitoring station is located at 37.172403° $N$ and 15.24655° E, as visible with a red dot in Fig. 1. The L4 satellite dataset provides a continuous temporal and spatial reference at a resolution of 1/100°. ME and RMSE were computed on a seasonal basis by comparing the satellite-measured Foundation temperature with the simulated temperature extracted and averaged from the first two layers (upper 2 m) between 00:00 and 02:00. In Fig. 2, the spatially averaged time series of the full dataset is presented, in order to observe the performance of the model over the whole time window under analysis. The model is able to accurately follow the surface temperature, with an higher positive bias observed during Summer 2022.

To illustrate the interseasonal performances and the spatial distribution of the error, in Fig. 3(a) it is visible how the model matches the satellite data with a maximum ME of 0.8 °C and a maximum RMSE of 1.0 °C during Summer periods. Moreover, in Fig. 3(b), the temporally averaged spatial error distribution for Summer periods is presented. The results indicate that the model follows the thermal evolution of the bay with high fidelity, though a localized tendency to overestimate temperature is observed in the immediate vicinity of the coastline.

The vertical consistency of the model was quantified using ME, RMSE, KGE and the Pearson correlation coefficient ($r$) (Table 1).

By looking at temperature, the model demonstrates high accuracy across all seasons, with $R$ values ranging from 0.95 to 1.00 and $KGE$ generally exceeding 0.76. This indicates that the thermal stratification and the depth of the thermocline are well-resolved. The Spring 2025 period shows a deviation in the $KGE$ (0.35), indicating a systematic bias during this window while the vertical structure remains correctly phased. This outlier mismatch has been found to be due to a bias present directly in the forcing oceanographic dataset in that period, thus not inferring a structural inacccuracy of the model. Regarding salinity, $R$ values remain consistently high (up to 0.99), suggesting a correct representation of the halocline structure. However, the $KGE$ is consistently lower than temperature comparisons. This is primarily a result of the low natural variance of salinity in the basin; when the observed variability is minimal, even a minor systematic bias, exemplified by the low RMSE values between 0.09 and 0.39 PSU, can lead to a low efficiency score.

**Table 1**
Summary of validation metrics for Temperature and Salinity profiles across different seasons (2024–2025). The metrics include Bias (ME), Root Mean Square Error (RMSE), Pearson Correlation Coefficient ($r$), and Kling–Gupta Efficiency (KGE).

| | | Temperature (°C) | | | | Salinity (PSU) | | | |
|---|---|---|---|---|---|---|---|---|---|
| Year | Season | ME | RMSE | $r$ | KGE | ME | RMSE | $r$ | KGE |
| 2024 | Spring (SP) | 0.01 | 0.15 | 0.95 | 0.92 | 0.26 | 0.28 | 0.83 | 0.07 |
| | Summer (SU) | 0.21 | 1.15 | 0.95 | 0.95 | −0.12 | 0.23 | 0.97 | 0.51 |
| | Autumn (A) | −0.33 | 0.51 | 0.97 | 0.76 | −0.39 | 0.39 | 0.84 | 0.65 |
| | Winter (W) | 0.29 | 0.35 | 1.00 | 0.88 | −0.15 | 0.18 | 0.99 | 0.38 |
| 2025 | Spring (SP) | −0.81 | 0.91 | 0.99 | 0.35 | −0.09 | 0.09 | 0.97 | 0.56 |
| | Summer (SU) | −0.16 | 0.50 | 0.99 | 0.98 | −0.24 | 0.27 | 0.98 | 0.59 |

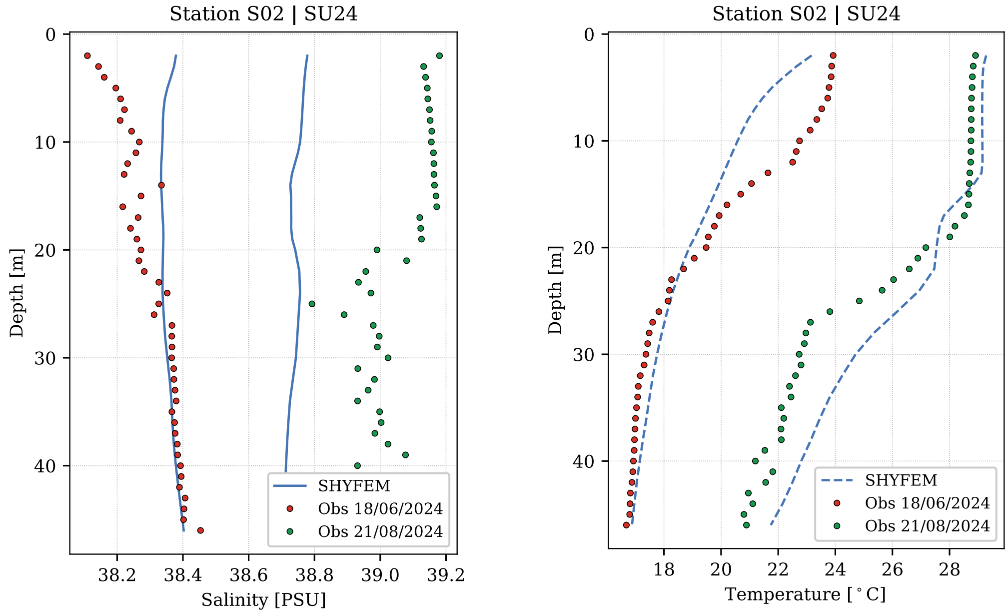


(a) Salinity (b) Temperature

**Fig. 4.** Comparison between ARPA in situ measurements (IDRONAUT OCEAN SEVEN 316) and SHYFEM-MPI profiles for Summer 2024 at station 37.172403° N, 15.24655° E.

Consequently, the high $R$ and low RMSE values provide a more representative assessment of the model's skill in reproducing the salinity field than the $KGE$ alone (see Fig. 4).

Ultimately, a multi-scale validation of the free-surface elevation was performed. Due to the lack of synchronous in-situ tide gauge measurements inside the basin, the model's sea level was validated against the Mediterranean Reanalysis dataset (Escudier et al., 2020) over the four-year simulation period (Fig. 5). This regional reanalysis product relies on a robust data assimilation scheme that continuously ingests vast streams of empirical observation, including satellite altimetry and field profiles. Consequently, it provides a highly reliable, state-of-the-art reference for large-scale physical balances and low-frequency variability across the Mediterranean basin. The results demonstrate a high consistency on a daily averaged scale (Bias= 0.047 m, RMSE= 0.062 m), confirming that the model correctly propagates the low-frequency macro-dynamics, atmospheric surges, and regional hydrodynamic signals from the open boundary into the bay. Conversely, at the high-frequency hourly scale, the comparison between the two datasets cannot provide a reliable indicator of the output quality. This is due to the fact that the regional reanalysis dataset is detided, which, combined with its coarse resolution (1/24°, ≈ 4 km) and smoothed bathymetry, prevents it from resolving either the astronomical tidal oscillations or the structural effects of the narrow artificial breakwaters enclosing the roadstead.

### *3.2. Seasonal averaged field*

An assessment of average quantities such as currents, temperature, and salinity (Fig. 6) has been performed. Regarding temperature, surface variations up to 2 °C has been observed between the inner bay and the open sea throughout the seasons. As expected for a semi-enclosed basin with limited water exchange and reduced capacity for heat dissipation, the port area is colder than the open sea during the winter and spring months, and warmer during summer and autumn. Salinity, on the other hand,

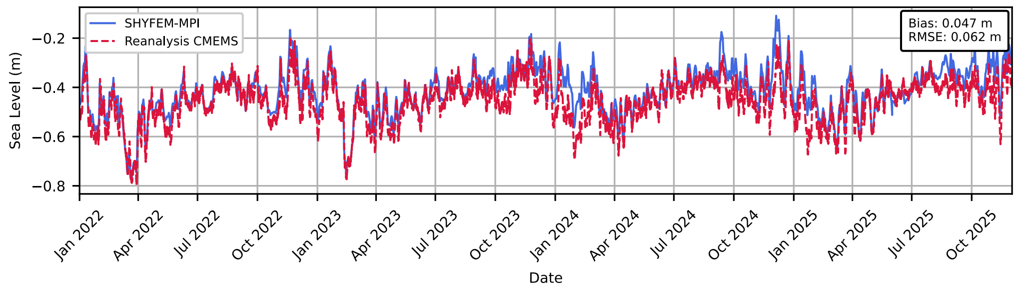


**Fig. 5.** Time series of simulated against reanalysis sea level over the 4 years under analysis. The comparison has been performed with respect to a suitable point located outside the Augusta bay (N 37° 11′ 33 E 15° 14′ 31.2)

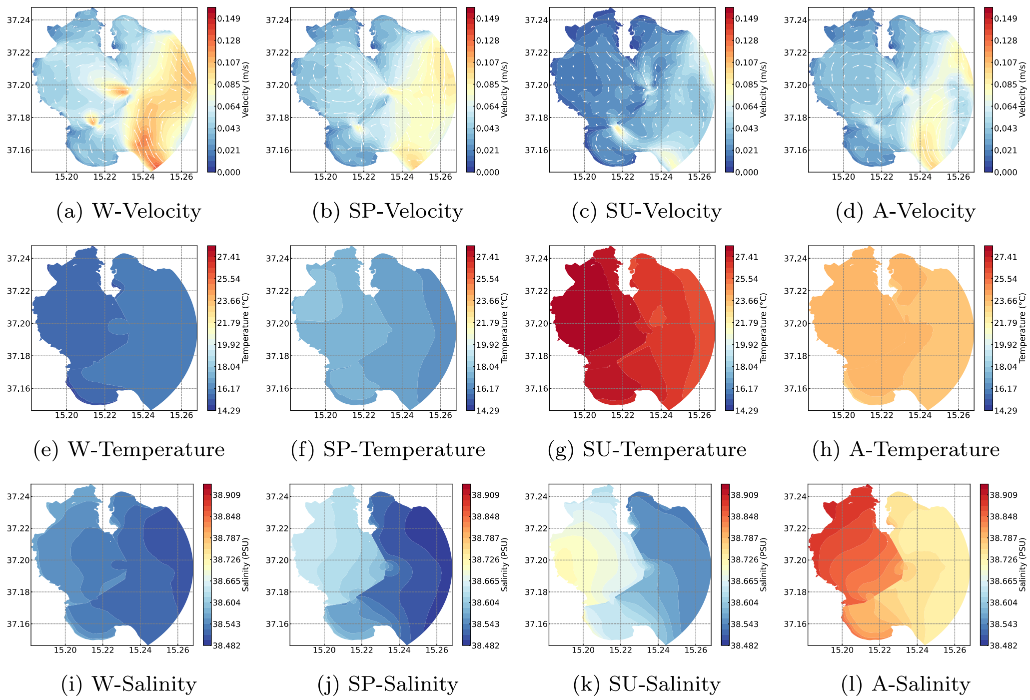


**Fig. 6.** Seasonal average surface currents (a–d), temperature (e–h) and salinity (i–l) in the domain, averaged over the two simulated years. From left to right in each row: Winter, Spring, Summer, and Autumn.

exhibits low spatial variability. Nevertheless, the presence of saltier water within the bay is consistent with expectations, likely due to enhanced evaporation. The most notable aspect concerns the average current patterns. The inner harbor is characterized by weak currents, with stagnation particularly concentrated in the northern sector of the bay, especially during summer. A persistent anticyclonic eddy can be identified across seasons (Fig. 6(a),6(b),6(c),6(d)), with a morphology likely influenced by the harbor entrances, which appear to act as conduits for mass and momentum exchange within the system. The relationship between incoming and outgoing flows and internal circulation will be further elucidated through comparison with vertical transects and EOF modes in Section 3.5. The south-to-north current observed outside the bay was previously documented in 2001 during the study by Raffa and Hopkins (2004) (Fig. 5, Transect IV). That study described the circulation reaching Augusta bay as being influenced by inputs from the Adriatic via the northern Ionian, the Atlantic inflow through the Strait of Sicily, the Tyrrhenian via the Strait of Messina, and the broader-scale Ionian circulation exchanging with the Levantine Basin. Also the works of Ciappa (2009) and Melaku Canu et al. (2015) identify northward currents resulting from the interplay between the Messina Rise Vortex and the Ionian Shelf Vortex. A detailed characterization of how this southern current connects to mesoscale structures lies beyond the scope of the present work and is part of an ongoing debate on how the Atlantic Waters spread from the western to the eastern Mediterranean.

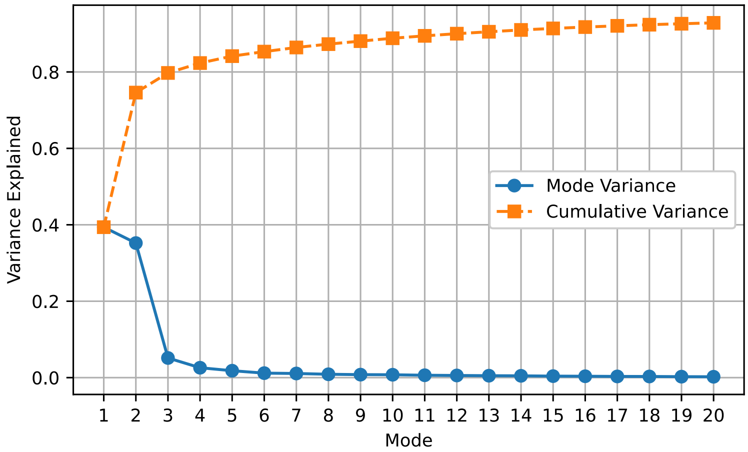


**Fig. 7.** EOF scree plot representing the magnitude of each mode (limited to the first 20 modes). The blue line shows the variance contribution of each mode, while the orange line indicates the cumulative variance captured as additional modes are included.

### 3.3. EOF structures

This section presents the results of applying EOF analysis to the generated dataset. When this type of analysis is employed for purposes other than Reduced Order Modeling, it is useful to select only a limited number of modes, not solely based on their cumulative energy contribution to the system, but rather on how rapidly the explained variance decreases from one mode to the next (a detailed discussion on these criteria can be found in the works of North et al. (1982) and Hannachi et al. (2007)). To better visualize this, Fig. 7 reports the contribution of the first 20 modes to the total system variance. Since the seasonal trends are nearly identical, only the autumn case is shown here for brevity. It can be observed that, after the third mode, the contribution to variance tends to a plateau. The EOF method thus generates modes that reflect less dominant and noisier dynamics, which are more difficult to interpret physically. For this reason, the subsequent analysis will consistently focus on the first three modes, which together account for approximately 80% of the total system variance.

In Fig. 8, the spatial structures of the modes across the seasons can be observed, describing the dynamics of the currents. It should be noted that, as is typical of EOF analysis, the spatial modes are modulated by the amplitude of their associated temporal modes, allowing for sign inversion when the coefficient is negative. This explains, for instance, some directions that may appear opposite to the seasonal mean patterns shown in Fig. 6. Focusing on the first two columns, which correspond to the leading modes contributing the largest portion of the system's energy (around 70%), a coherent flow can be observed for both, deviated only near the coast, with a persistent 90° direction shift between them across the seasons. The direction, however, changes seasonally, suggesting a dependence on wind forcing, which will be further investigated in Section 3.4. Mode 3, on the other hand, highlights a residual motion modulated by the two openings and amplified in proximity to the coast, showing the effect of coast topology in establishing the eddy observed in the mean fields. An interesting feature is that even from Fig. 6 it is clear how the water exchange with the open sea can suppress or enhance certain dynamics. In summer, for example, mode 3 is dominated by the vortex, which represents a weaker-energy feature during other seasons, precisely because the mass and momentum introduced by the openings are absent; conversely, in winter, this inlet is clearly visible and highly energetic. A more detailed analysis of this relationship will be presented in next sections, related to baroclinic effects, open-sea currents and interannual comparison.

### 3.4. Wind and EOF

Given the variable wind direction reflected in the first two modes, a comparison was made between the spatial and temporal EOF modes and the wind components used to force the model. Fig. 9 shows the wind roses at 10 m, representing the wind distribution (in meteorological convention) for each season. It should be noted that, due to the significant difference in resolution between the atmospheric grid and the ocean model grid, the constructed model is forced with a spatially uniform wind field over the entire bay. This procedure filters out and removes possible effects of coastal sheltering. During the period simulated, wind appears to be mainly coming from NW-W, with higher wind speed in Winter (up to 16 m/s) and lower in Summer (rarely exceeding 9 m/s) with low interannual variability. This is in line with analysis previously made in the area (Marchis et al., 2014).

A visual comparison between the first EOF mode and the prevailing wind direction (either most frequent or most energetic) does not reveal a clear or consistent correlation. This suggests that the representation of wind forcing within the system may be distributed across both the first and second modes. To investigate this hypothesis quantitatively, we performed statistical analyses, including Pearson correlation and regression analysis. The comparison was carried out by reconstructing the velocity field using only the first two modes, thereby isolating the wind effect within a variable flow field, since the spatial modes are linearly combined with their corresponding temporal modes.

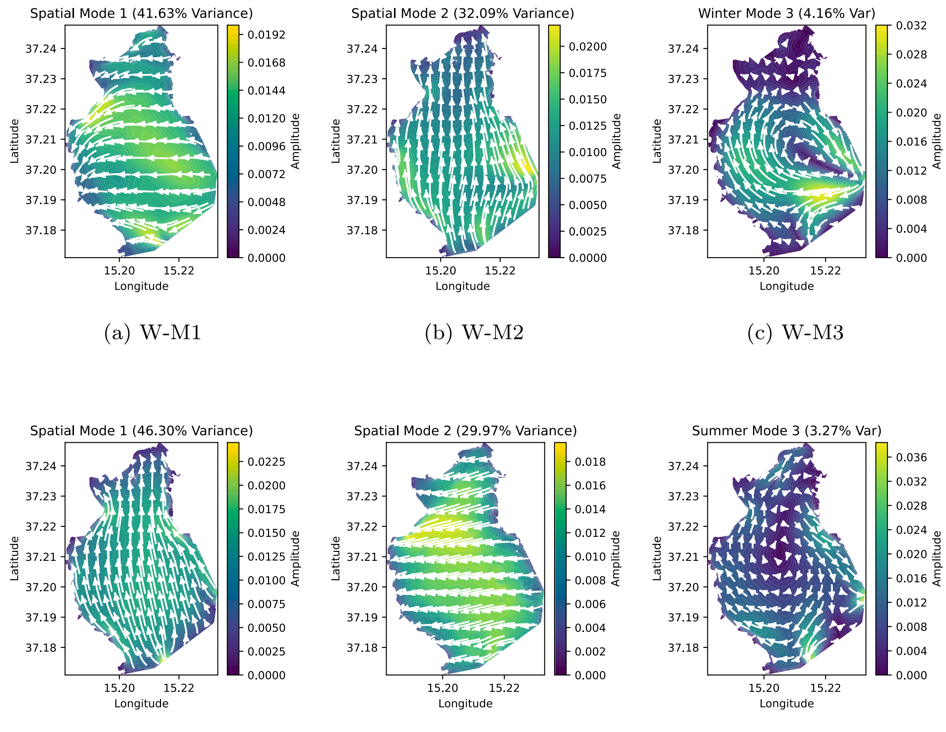


(a) W-M1 (b) W-M2 (c) W-M3

(d) SU-M1 (e) SU-M2 (f) SU-M3

**Fig. 8.** First three EOF spatial modes extracted for summer and winter seasons. Arrows indicate current direction (temporal modulation can invert it), while the colorbar refers to velocity magnitude. Captions indicate the season and the mode number indicated.

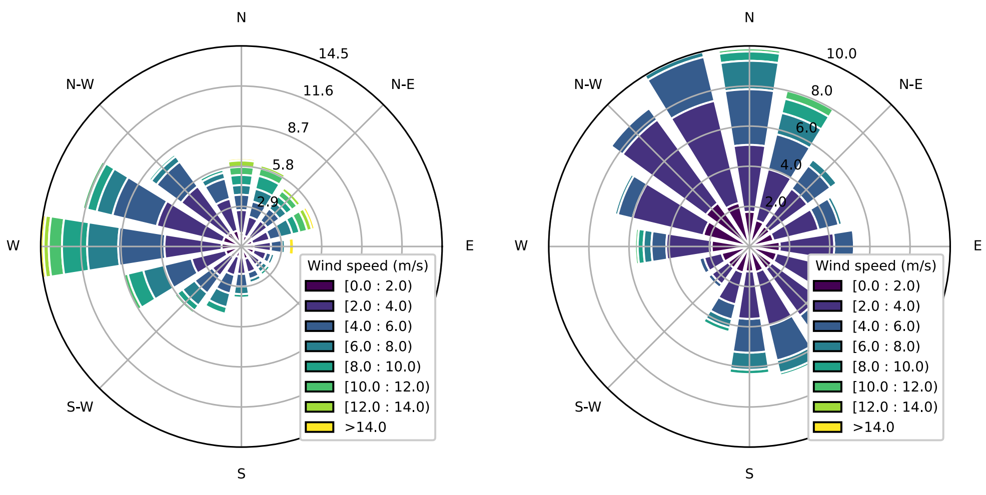


(a) W (b) SU

**Fig. 9.** Wind roses obtained from the dataset used to force the simulations. Captions indicate the season code to which they refer.

Table 2 summarizes the key quantitative metrics by season. In this context, given the large dataset available for the comparison, all analyses yielded p-values well below the conventional threshold of 0.05, thereby ensuring the statistical significance of the reported values.

The statistical analysis conducted between wind observations and surface currents reconstructed via EOF reveals a strong linear relationship, particularly for the zonal (East–West, U) component. Pearson correlation values for the U component exceed 0.90 in winter and spring and remain high ( 0.71) during summer, a season in which wind intensity, as foreseen before, is not high enough to influence so clearly the current direction. The meridional (North–South, V) component also shows significant correlation, albeit

**Table 2**
Seasonal statistics of the wind–current relationship in Augusta Harbor. Pearson correlation coefficients ($r_U$, $r_V$) quantify the linear dependence between wind and current velocity component, while coefficients of determination ($R_u^2$, $R_v^2$) assess the proportion of variance in currents explained by wind forcing.

| Season | $Corr_U$ | $Corr_V$ | $R_u^2$ | $R_v^2$ | $N_{eff}$ | $p_{value}$ |
|---|---|---|---|---|---|---|
| Winter | 0.938 | 0.871 | 0.880 | 0.758 | 105 | $\ll 0.05$ |
| Spring | 0.886 | 0.808 | 0.786 | 0.652 | 194 | $\ll 0.05$ |
| Summer | 0.710 | 0.765 | 0.504 | 0.585 | 428 | $\ll 0.05$ |
| Autumn | 0.906 | 0.855 | 0.820 | 0.730 | 221 | $\ll 0.05$ |

slightly lower, ranging between approximately 0.76 and 0.87 across seasons. In summary, the results indicate that surface currents in Augusta Harbor are strongly wind-driven on synoptic and sub-synoptic timescales, as also previously demonstrated by Marchis et al. (2014). The response varies slightly with season, but the overall coupling remains robust, especially for the zonal component. This dynamic is modulated by both seasonal atmospheric variability and the harbor's structural configuration. The shift of 90° is a non-physical artifact generated through the EOF analysis, in order to represent the time-varying wind field, that can explain almost 70% of the variance of the whole system's dynamics. A similar behavior of the reconstructed modes forced by winds has also been observed in Elken et al. (2011).

### 3.5. Vertical transects

To better capture baroclinic effects and extend the analysis beyond surface circulation, two vertical transects were defined, as shown in Fig. 1. The first, named *Scirocco*, crosses the corresponding southern opening of the bay, while the second, *Levante*, extends eastward toward the open sea. These sections allow the assessment of the interaction between the inner and outer parts of the bay in terms of density and velocity structure. For simplicity, the analysis focuses on the summer and winter conditions, when stratification and circulation show the greatest contrast. For each transect, the in-plane velocity component was considered: zonal for Levante and meridional for Scirocco. Fig. 10 presents the seasonal mean density fields. The difference between summer and winter stratification is evident. In summer, strong thermal stratification develops, forming a stable water column that limits horizontal exchange through baroclinic inhibition. Horizontal density gradients are confined to the uppermost layers, and weak wind forcing further contributes to stagnant conditions within the bay (Fig. 10(c),10(g)). During winter, colder and denser offshore waters intrude through the openings, creating horizontal density gradients that enhance the exchange between the bay and the open sea (Fig. 10(a),10(e)). This leads to surface inflow and compensating deep outflow.

Velocity transects support this interpretation. The Scirocco opening shows weaker exchanges with the open sea (Fig. 10(f)), consistent with smaller density contrasts and weaker currents, as also reported by Marchis et al. (2014). In contrast, the Levante opening displays stronger winter density gradients and a more active circulation, characterized by surface inflow and downwelling of inner-bay waters (Fig. 10(b)). This circulation promotes mass exchange and vertical mixing, strengthening the renewal of inner waters. In summer, stratification suppresses both baroclinic circulation and mixing, resulting in more diverse but weaker exchange patterns (Fig. 10(h),10(d)).

To further characterize the vertical stability of the water column along the transects, we computed the Brunt–Väisälä frequency ($N^2$) profiles, in Fig. 11 at selected inspection points (Fig. 1, left). The Brunt–Väisälä frequency is defined as:

$$N^2 = -\frac{g}{\rho}\frac{d\rho}{dz} \tag{2}$$

where: $N$ is the Brunt–Väisälä frequency ($s^{-1}$), $g$ is the acceleration due to gravity (m $s^{-2}$), $\rho$ is the seawater density ($Kg/m^3$) and $\frac{d\rho}{dz}$ is the vertical gradient of density. When $N^2 > 0$, the water column is statically stable, whereas $N^2 < 0$ indicates static instability. These profiles provide a quantitative measure of stratification and allow the identification of layers prone to baroclinic activity. For each transect, $N^2$ was evaluated at three representative locations along the section: near the inner bay, mid-transect, and close to the outer opening. Seasonal mean profiles highlight the contrast between summer and winter conditions: in summer, $N^2$ maxima are concentrated near the pycnocline, indicating strong stratification in the upper 10–50 m, whereas in winter, the profiles are more homogeneous with lower maxima, reflecting weaker vertical density gradients as expected.

### 3.6. EOF of density transects

To better investigate the vertical behavior of the water column on an inter-seasonal scale, EOFs were computed for the vertical density fields along the two transects. Analogously to the analysis of the velocity field, only the first three modes of the vertical density fields are considered. The density anomaly relative to the mean field suggests that most of the variance, both in summer and winter, is concentrated in the seasonal cycle of heating and cooling, which respectively strengthens or weakens the water column stratification. As an example, Fig. 12(a) shows the first mode, computed over the whole period, which accounts for 92% to 98% of the total variance, depending on the season. The temporal evolution of the mode (Fig. 12(b)) clearly indicates a counterphase behavior with respect the surface temperature. During summer months, the amplitude of the mode will become negative in order to reduce surface density, thus strengthening stratification.

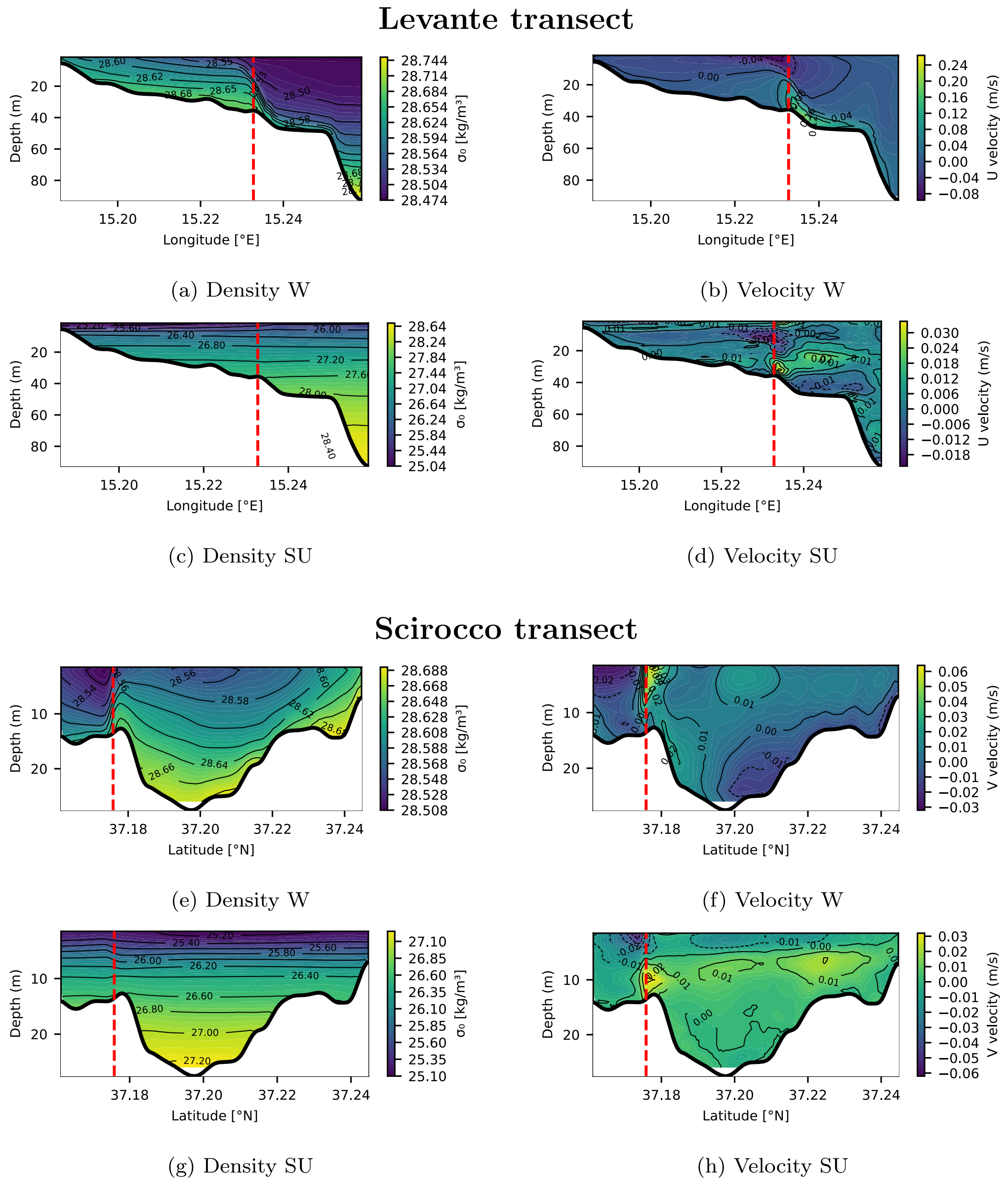


**Fig. 10.** Seasonal mean density and in-plane velocity fields for winter and summer along each transect. Captions indicate field and season code. Red lines indicate the corresponding opening.

Mode 2 during winter captures the horizontal density gradients between the inner and outer bay (Fig. 13). In the Levante transect, this mode does not display a specific dominant frequency but instead represents a bulk dense-water outflow that varies in intensity over time (Fig. 13(a)). In the Scirocco transect (Fig. 13(c)), the situation is different: a recirculation motion is observed, exhibiting both daily and tidal frequencies, inducing vertical mixing near the northern, shallower portion of the bay, and resulting in a downwelling from the north. During summer, Mode 2 represents the daily strengthening and weakening of the stratified water column in both transects, driven by surface solar heating (Fig. 13(b),13(d)).

In winter, Mode 3 along the Scirocco transect (Fig. 14(c)) indicates the inflow of denser water into the bay through the opening, accompanied by upwelling in the northern area. Along the Levante transect, Mode 3 instead exhibits an oscillatory component with daily and tidal periodicities, associated with the water flux through the opening (Fig. 14(a)). This behavior is influenced by downwelling from the western part of the bay, which penetrates deeper along the slope, consistent with near-zero spatial coefficients across most of the outer domain.

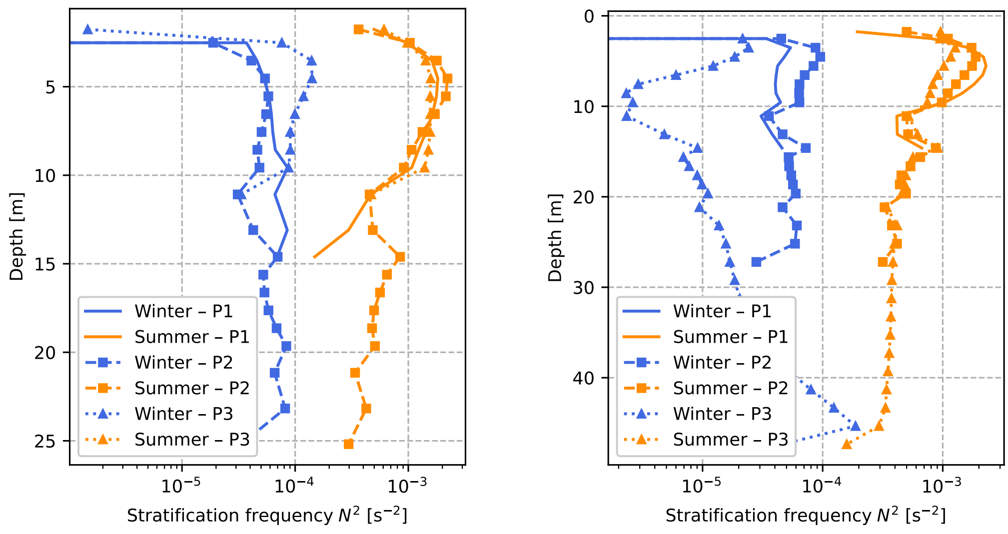


(a) N2 profile Levante

(b) N2 profile Scirocco

**Fig. 11.** N2 profiles for Levante transect (a) and Scirocco transect (b) for summer and winter seasons. Points are indicated in Fig. 1, left. Point P1 is the inner point, point P2 is the mid point, and point P3 indicates the outer point.

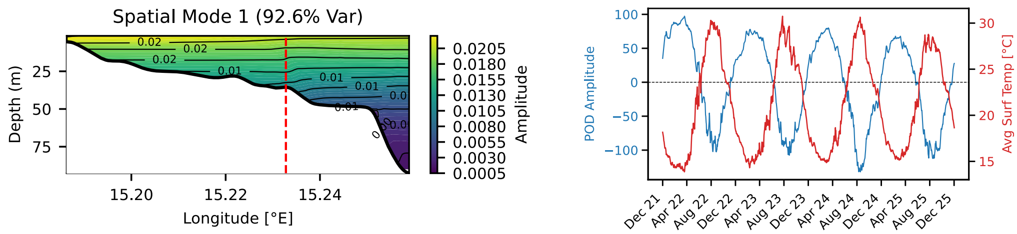


(a) Spatial structure

(b) Temporal structure

**Fig. 12.** Spatial (a) and temporal structure (b) of Mode 1, computed over the whole time window analyzed. Only Levante transect has been shown for clarity.

During summer, Mode 3 along the Levante transect identifies two distinct layers, around 10 and 50 m depth, which alternately destabilize or reinforce the water column on daily and tidal timescales (Fig. 14(b)). Along the Scirocco transect, the same mode primarily affects the upper 10 m of the water column (Fig. 14(d)), corresponding to the pycnocline, which during summer is located between 5 and 10 m (Fig. 11). Therefore, the mode highlights its presence in influencing stratification stability: the northern side and the outer part of the transect tend to become denser and lighter, respectively, suggesting the excitation of a recirculation mechanism driven by the sinking of surface waters.

### *3.7. Interannual variability*

Quantifying the interannual variability of seasonal patterns and Empirical Orthogonal Function (EOF) structures can strengthen previous findings and provide further insights into the primary drivers governing the coastal site. For instance, Fig. 15 illustrates that during both summer and winter months, the year 2025 exhibits a more intense external current impinging on the roadstead. This intensification reduces water stagnation and enhances the flux across the two inlets. It should be noted that, within the simulated dataset, the intensity of the northward-flowing current increases monotonically over the years.

The strengthening of the offshore current is reflected in Fig. 16, which presents the calculated mean water fluxes through the inlets. Indeed, from 2022 to 2025, both inflowing and outflowing net fluxes increase in magnitude as a result of the strengthened external circulation. During the winter months, the exchange is further promoted by the previously observed lack of stratification; specifically, the net flux through the Levante inlet is dominated by outflowing currents in the deeper layers of the water column. The dominant role in water exchange dynamics of the Levante opening has already been observed by Marchis et al. (2014), yielding water mass-flow values that are appreciably closer to the results of this paper and the one of Lisi et al. (2009). However, in the

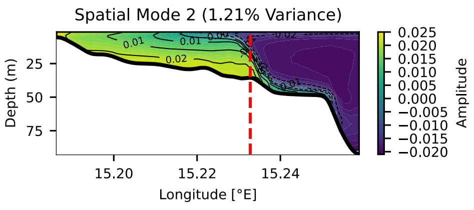


(a) Levante W

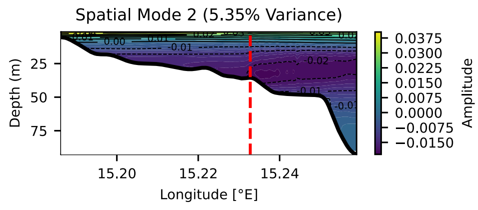


(b) Levante SU

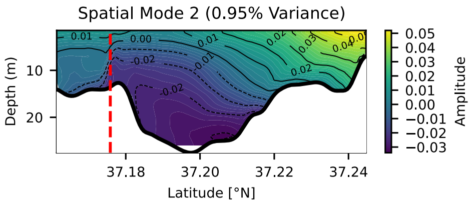


(c) Scirocco W

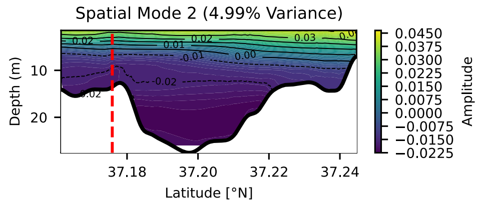


(d) Scirocco SU

**Fig. 13.** Spatial structures of Mode 2 for Winter (left column) and Summer (right column), for the Levante transect (top row) and the Scirocco transect (bottom row).

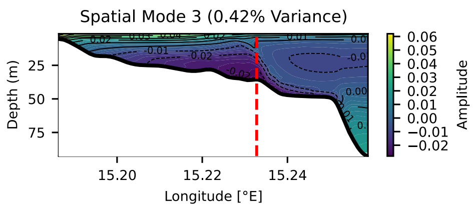


(a) Levante W

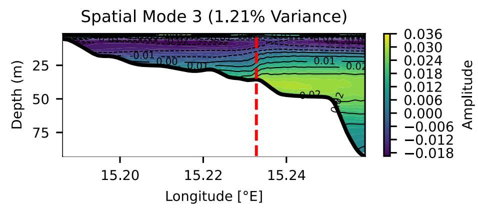


(b) Levante SU

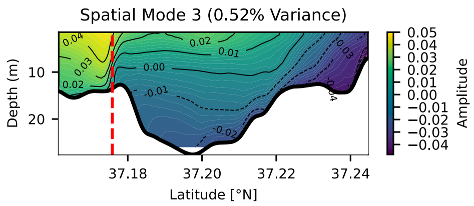


(c) Scirocco W

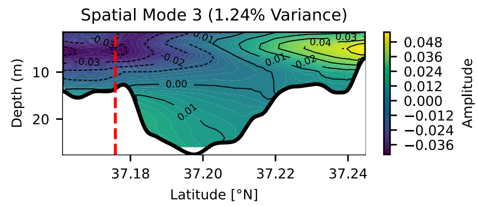


(d) Scirocco SU

**Fig. 14.** Spatial structures of Mode 3 for Winter (left column) and Summer (right column), for the Levante transect (top row) and the Scirocco transect (bottom row).

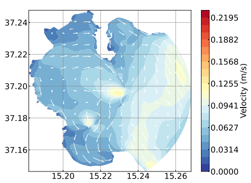

(a) W22

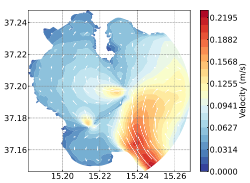

(b) W25

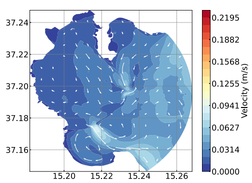

(c) SU22

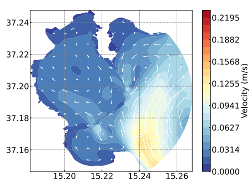

(d) SU25

**Fig. 15.** Interannual comparison of surface current quiver plots over winter and summer periods.

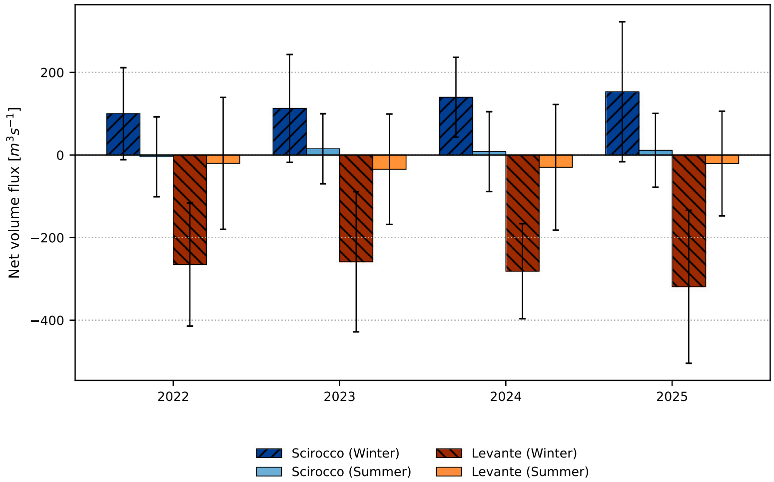


**Fig. 16.** Net fluxes through Scirocco and Levante inlets over the years, grouped by season. Error bars represent the standard deviation computed for each period.

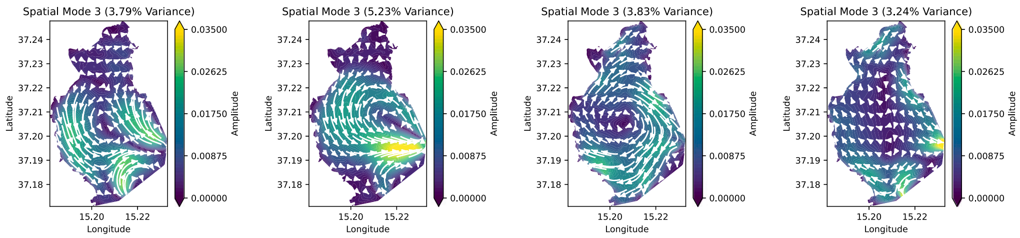


(a) W22 (b) W25 (c) SU22 (d) SU25

**Fig. 17.** Interannual comparison of mode 3 surface current quiver plot over winter and summer periods.

present study it has been possible to deepen the analysis by exploring which drivers influence the exchange on an interannual and interseasonal basis. In fact, this mechanism appears decoupled from interannual wind variability, which is found to be negligible and inconsistent with the observed trends. Consequently, it is crucial to assert that a proper characterization of external currents is fundamental when calculating flushing and residence times for pollutants discharged into the basin.

The interannual variability of the EOF modes was also examined. Modes 1 and 2 are omitted from the following plots for brevity, as they primarily represent the response to wind stress. However, it was observed that the combined explained variance of these two modes consistently remains near 70%, with higher averages during summer periods. In these months, the reduced water exchange with the open sea diminishes the influence of the inlets on the internal variance of the roadstead. Conversely, Mode 3, shown in Fig. 17, appears consistent across seasons. This mode identifies a residual motion of the water mass influenced by coastal morphology and modulated by the intensity of the flux through the inlets, particularly the Levante inlet. Specifically, comparing the winters of 2022 and 2025, the latter being characterized by stronger external forcing, it is evident that the vortex becomes increasingly dominated by the influence of the Levante inlet. In contrast, during the summer, this feature may persist as a residual circular motion (as in 2022) or undergo structural breakdown due to increased water input from the inlets. These findings reinforce the hypothesis that the anticyclonic vortex identified in the seasonal mean currents varies on both interannual and seasonal scales, depending on the coupling with the offshore marine environment.

### *3.8. Discussion and limitations*

The combined application of high-resolution numerical modeling and EOF analysis has allowed for a detailed deconstruction of the hydrodynamics within Augusta Bay, and it is worth discussing implications of the results observed and the model limitations. A key finding of this study is a decoupling between surface circulation drivers and water column exchange mechanisms. While surface currents are highly responsive to wind variability, as evidenced by the high correlation between wind vectors and the first two velocity EOF modes, the renewal of bay waters is predominantly controlled by the seasonal stratification cycle. This implies that during summer, despite wind-induced surface mixing, stratification acts as a barrier, damping water exchange, effectively isolating the deeper layers and potentially trapping pollutants released near the seabed. Conversely, winter conditions favor a baroclinic setup that enhances flushing efficiency through the Levante and Scirocco openings.

From a methodological perspective, the EOF analysis proved superior to traditional seasonal averaging in identifying these mechanisms. While seasonal means (Fig. 6) highlight persistent features like the anticyclonic eddy, they tend to smooth out the dynamic response to transient forcing. The EOF decomposition successfully isolated and quantified in terms of variance explained the wind-driven component from the topographic steering, providing a clearer picture of how the basin responds to external energy inputs.

However, this study is subject to certain limitations that must be acknowledged. First, the model validation relies primarily on temperature and salinity observations. It must be highlighted that continuous in-situ vertical velocity profiles (e.g., via ADCP arrays) are extremely rare and notoriously difficult to acquire for validation purposes in heavily modified, restricted industrial harbors. The lack of long-term continuous current measurements for the simulated period limits the direct validation of the vertical velocity structures. While the circulation patterns described here are consistent with physical principles and previous regional literature (Marchis et al., 2014), dedicated field campaigns would be beneficial to further constrain the model's internal dynamics.

Furthermore, as explored by Marchis et al. (2014), astronomical tides exhibit a relatively low contribution to the overall surface current variance in this basin. Consequently, potential inaccuracies in the spatial configuration of the wind forcing representation may introduce a much more critical limitation to the true physical predictability of the inner-harbor currents than tidal discrepancies. Regarding sea level observations, direct in-situ gauge measurements remain highly scarce in the area and are strictly limited to short-term, isolated research field campaigns.

Nevertheless, we maintain a high degree of confidence in the simulated baroclinic circulation pathways; the thermohaline structure has been explicitly validated across multiple seasons against ARPA vertical profiles, and within low-tidal environments like the Mediterranean Sea, any error introduced by unverified astronomical tidal phases is minimized, ensuring that the primary density-driven patterns are correctly captured.

Secondly, the atmospheric forcing applied to the model assumes a spatially uniform wind field over the bay, derived from the ECMWF dataset. As noted in Section 3.4, this approach neglects local sheltering effects caused by the surrounding orography and urban infrastructure. While this approximation is acceptable for capturing the dominant seasonal and synoptic variability, it likely oversimplifies the wind stress distribution near the coastlines, potentially affecting the resolution of small-scale coastal eddies. However, as noted by Lewis et al. (2019), the accuracy of the surface energy budget, particularly the representation of cloud cover and its impact on shortwave radiation, often exerts a first-order control on the quality of SST simulations, exceeding the relative impact of wind forcing resolution in near-coastal environments.

Lastly, the strategic comparison of our model output against the regional reanalysis dataset was specifically targeted to evaluate the model's capacity to capture low-frequency, de-tided spatial signals on a daily scale. We cannot, however, employ this macroscale reanalysis for a rigorous high-frequency or hourly velocity validation; the intrinsic horizontal coarseness and localized bathymetric approximations of the reanalysis product near highly narrow breakwaters render it unreliable for resolving local structural flows inside a topologically constrained embayment.

Despite these limitations, the results provide a valuable baseline for environmental management. The identification of summer stagnation periods suggests that monitoring and remediation activities for the SIN should account for the reduced dilution capacity of the bay during stratified months. A future model with tracer tracking could provide useful measurements regarding residence time of pollutants and water renewal of the basin.

## 4. Conclusions

This study has applied a high-resolution numerical model and EOF analysis to characterize the hydrodynamic features of Augusta Bay over a four-year period. The results indicate that the circulation within the basin is influenced by a combination of atmospheric forcing, seasonal density variations, and the local bathymetric configuration. The EOF decomposition of the surface velocity field showed that the first two modes of variability are closely related to wind stress, reflecting a clear seasonal pattern in current intensity. While these modes explain a significant portion of the surface variance, the analysis suggests that deeper water exchange is more directly controlled by the annual stratification cycle. The examination of vertical density structures confirmed that the water column remains stratified during the summer months, which appears to limit the efficiency of water renewal through the bay's openings. In contrast, the reduction of stratification in winter supports more active baroclinic circulation. Furthermore, the interannual comparison highlighted that the intensity of the external Ionian current plays a role in determining the magnitude of exchange through the inlets, independent of local wind conditions. The identification of a persistent anticyclonic structure through the third velocity mode further illustrates the effect of the basin's geometry on internal circulation. These results offer a detailed physical framework for understanding the transport mechanisms in Augusta Bay and demonstrate the utility of EOF analysis for isolating specific components of coastal circulation. This information may be useful for the development of future management and remediation strategies for this industrial coastal site.

**Table A.3**
Description of model parameters and symbols.

| Group | Symbol | Description |
|---|---|---|
| Grid | $n_{\text{nodes}}$ | Total number of computational nodes |
| | $n_{\text{elem}}$ | Total number of triangular elements |
| | $\delta s/\Delta S$ | Minimum and maximum horizontal resolution |
| | $n_z$ | Total number of vertical layers |
| | $\Delta z_i$ | Vertical layer thickness |
| Subgrid | $\nu_H$ | Background horizontal eddy viscosity |
| Processes | $k_{H,T}/k_{H,S}$ | Horizontal temperature and salinity diffusivity |
| | turb | Vertical turbulence closure scheme |
| | $\nu_b/k_b$ | Molecular eddy viscosity and diffusivity |
| Friction | $C_D$ | Wind stress drag coefficient |
| | $C_B$ | Bottom drag coefficient formulation |
| | $\lambda$ | Bottom friction parameter |
| Ad. Scheme | | Formalization of the advection scheme employed |
| Air-sea Fluxes | | Formalization for surface fluxes correction |
| Time | $\text{date}_0$ | Simulation start date (YYYYMMDD) |
| | $t_{\text{spinup}}$ | Model spin-up period |
| | $\Delta t$ | Temporal integration step |

## CRediT authorship contribution statement

**Diego Bindoni:** Writing – original draft, Visualization, Validation, Methodology, Investigation, Formal analysis, Data curation, Conceptualization. **Jacopo Alessandri:** Writing – review & editing, Supervision, Conceptualization. **Ivan Federico:** Writing – review & editing, Supervision, Conceptualization. **Antonella Abbà:** Writing – review & editing, Supervision, Conceptualization.

## Funding

This research did not receive any specific grant from funding agencies in the public, commercial, or not-for-profit sectors.

## Declaration of competing interest

The authors declare that they have no known competing financial interests or personal relationships that could have appeared to influence the work reported in this paper.

## Acknowledgments

The research activities described in this paper were carried out with contribution of the NextGenerationEU funds within the National Recovery and Resilience Plan (PNRR), Mission 4, Component 2 - From Research to Business (M4C2), Investment Line 3.3 - Introduction of innovative doctorates responding to the innovation needs of companies and promoting the hiring of researchers by companies, Project *CO2 sequestration in ocean: numerical simulations and experiments*. We would also like to remark the contribution given by ARPA Sicilia in making available in situ vertical profiles of temperature and salinity used in Section 3.1.

## Appendix. Model configuration and settings

Tables A.3 and A.4 summarizes the numerical parameters and physical settings used for the SHYFEM-MPI model simulation.

## Data availability

Data will be made available on request.

**Table A.4**
Numerical values and formulations for the Augusta Bay simulation.

| Parameter | Value/Setting |
|---|---|
| $n_{nodes}$ | 11 879 |
| $n_{elem}$ | 22 802 |
| $\delta s/\Delta S$ | 40 m/1000 m |
| $n_z$ | 45 |
| $\Delta z_i$ | 0.5 m (first layer), 1 m (until 20 m), 2 m (until 60 m), then stepwise increased |
| $\nu_H$ | 0.2 (Smagorinsky model for horizontal diffusion) |
| $k_{H,T}/k_{H,S}$ | 0.2 |
| turb | $k$-$\epsilon$ (GOTM) |
| $\nu_b$ | $10^{-6}$ m$^2$/s |
| $k_b$ | $10^{-7}$ m$^2$/s |
| $C_D$ | 0.0025 with Hellerman and Rosenstein formulation (Hellerman and Rosenstein, 1983) |
| $C_B$ | Roughness length ($\lambda$) logarithmic formulation |
| $\lambda$ | 0.01 |
| Ad. Scheme | TVD (Total Variation Diminishing) |
| Air-sea Fluxes | Formalization from Pettenuzzo et al. (2010) |
| date$_0$ | 2021–11–20 |
| $t_{spinup}$ | 10 days |
| $\Delta t$ | Variable (avg ≈ 120 s) |

## References


Ausili, A., Bergamin, L., Romano, E., 2020. Environmental status of Italian Coastal Marine Areas affected by long history of contamination. Front. Environ. Sci. 8, http://dx.doi.org/10.3389/fenvs.2020.00034.

Benedetti, M., Romano, E., Ausili, A., Fattorini, D., Gorbi, S., Maggi, C., Salmeri, A., Salvagio Manta, D., Sesta, G., Sprovieri, M., Regoli, F., 2022. 10-Year time course of hg and organic compounds in augusta bay: Bioavailability and biological effects in marine organisms. Front. Public Health 10, http://dx.doi.org/10.3389/fpubh.2022.968296, URL: https://www.frontiersin.org/journals/public-health/articles/10.3389/fpubh.2022.968296.

Buongiorno Nardelli, B., Tronconi, C., Pisano, A., Santoleri, R., 2013. High and ultra-high resolution processing of satellite sea surface temperature data over southern European seas in the framework of myocean project. Remote Sens. Environ. 129, 1–16. http://dx.doi.org/10.1016/j.rse.2012.10.012.

Burchard, H., Bolding, K., 2001. Comparative analysis of four second-moment turbulence closure models for the oceanic mixed layer. J. Phys. Oceanogr. 31 (8), 1943–1968. http://dx.doi.org/10.1175/1520-0485(2001)031<1943:CAOFSM>2.0.CO;2, URL: https://journals.ametsoc.org/view/journals/phoc/31/8/1520-0485_2001_031_1943_caofsm_2.0.co_2.xml.

Causio, S., Federico, I., Jansen, E., Mentaschi, L., Ciliberti, S.A., Coppini, G., Lionello, P., 2024. The black sea near-past wave climate and its variability: a hindcast study. Front. Mar. Sci. 11, http://dx.doi.org/10.3389/fmars.2024.1406855.

Ciappa, A.C., 2009. Surface circulation patterns in the sicily channel and ionian sea as revealed by MODIS chlorophyll images from 2003 to 2007. Cont. Shelf Res. 29 (17), 2099–2109. http://dx.doi.org/10.1016/j.csr.2009.08.002.

Copernicus Marine Service, 2025. Mediterranean sea high resolution and ultra high resolution sea surface temperature analysis. http://dx.doi.org/10.48670/moi-00172, Accessed 22 May 2025.

Elken, J., Nomm, M., Lagemaa, P., 2011. Circulation patterns in the gulf of Finland derived from the EOF analysis of model results. Boreal Environ. Res. 16, 84–102.

EMODnet Bathymetry Consortium, 2024. EMODnet digital bathymetry (DTM 2024). http://dx.doi.org/10.12770/cf51df64-56f9-4a99-b1aa-36b8d7b743a1, Dataset; Accessed YYYY-MM-DD.

Escudier, R., Clementi, E., Omar, M., Cipollone, A., Pistoia, J., Aydogdu, A., Drudi, M., Grandi, A., Lyubartsev, V., Lecci, R., Cretí, S., Masina, S., Coppini, G., Pinardi, N., 2020. Mediterranean Sea Physical Reanalysis (CMEMS MED-Currents) (Version 1). http://dx.doi.org/10.25423/CMCC/MEDSEA_MULTIYEAR_PHY_006_004_E3R1.

E.U. Copernicus Marine Service Information (CMEMS), 2025. MEDSEA_ANALYSISFORECAST_PHY_006_013. http://dx.doi.org/10.48670/mds-00359, (Accessed 05 January 2025).

European Centre for Medium-Range Weather Forecasts, 2025. Integrated forecasting system: Changes to the ECMWF model. URL: https://www.ecmwf.int/en/forecasts/documentation-and-support/changes-ecmwf-model. (Accessed 13 October 2025).

Fanelli, C., Ciani, D., Pisano, A., Buongiorno Nardelli, B., 2024. Deep learning for super-resolution of mediterranean sea surface temperature fields. Ocean. Sci. 20 (4), 1035–1052. http://dx.doi.org/10.5194/os-20-1035-2024.

Hannachi, A., Jolliffe, I.T., Stephenson, D.B., 2007. Empirical orthogonal functions and related techniques in atmospheric science: A review. Int. J. Climatol. 27 (9), 1119–1152. http://dx.doi.org/10.1002/joc.1499.

Hellerman, S., Rosenstein, M., 1983. Normal monthly wind stress over the world ocean with error estimates. J. Phys. Oceanogr. 13 (7), 1093–1104. http://dx.doi.org/10.1175/1520-0485(1983)013<1093:NMWSOT>2.0.CO;2, URL: https://journals.ametsoc.org/view/journals/phoc/13/7/1520-0485_1983_013_1093_nmwsot_2_0_co_2.xml.

Lewis, H.W., Siddorn, J., Castillo Sanchez, J.M., Petch, J., Edwards, J.M., Smyth, T., 2019. Evaluating the impact of atmospheric forcing and air–sea coupling on near-coastal regional ocean prediction. Ocean. Sci. 15 (3), 761–778. http://dx.doi.org/10.5194/os-15-761-2019, URL: https://os.copernicus.org/articles/15/761/2019/.

Lisi, I., Taramelli, A., Di Risio, M., Cappucci, S., Gabellini, M., 2009. Flushing efficiency of augusta harbour (Italy). J. Coast. Res. 56, 841–845.

Marchis, M.D., Freni, G., Napoli, E., 2014. Three-dimensional numerical simulations on wind- and tide-induced currents: The case of Augusta Harbour (Italy). Comput. Geosci. 72, 65–75. http://dx.doi.org/10.1016/j.cageo.2014.07.003.

Melaku Canu, D., Solidoro, C., Bandelj, V., Quattrocchi, G., Sorgente, R., Olita, A., Fazioli, L., Cucco, A., 2015. Assessment of oil slick hazard and risk at vulnerable coastal sites. Marine Poll. Bull. 94 (1), 84–95. http://dx.doi.org/10.1016/j.marpolbul.2015.03.006, URL: https://www.sciencedirect.com/science/article/pii/S0025326X15001381.

Micaletto, G., Barletta, I., Mocavero, S., Federico, I., Epicoco, I., Verri, G., Coppini, G., Schiano, P., Aloisio, G., Pinardi, N., 2022. Parallel implementation of the SHYFEM (System of HydrodYnamic Finite Element Modules) model. Geosci. Model. Dev. 15, 6025–6046. http://dx.doi.org/10.5194/gmd-15-6025-2022.

Morales-Marín, L.A., French, J.R., Burningham, H., 2017. Implementation of a 3D ocean model to understand upland lake wind-driven circulation. Environ. Fluid Mech. 17 (6), 1255–1278. http://dx.doi.org/10.1007/s10652-017-9548-6.

North, G.R., Bell, T.L., Cahalan, R.F., Moeng, F.J., 1982. Sampling errors in the estimation of empirical orthogonal functions. Mon. Weather Rev. 110 (7), 699–706. http://dx.doi.org/10.1175/1520-0493(1982)110<0699:SEITEO>2.0.CO;2, URL: https://journals.ametsoc.org/view/journals/mwre/110/7/1520-0493_1982_110_0699_seiteo_2_0_co_2.xml.

Pearson, K., 1895. Note on Regression and Inheritance in the Case of Two Parents. Proc. R. Soc. Lond. Ser. I 58, 240–242.

Pettenuzzo, D., Large, W.G., Pinardi, N., 2010. On the corrections of ERA-40 surface flux products consistent with the Mediterranean heat and water budgets and the connection between basin surface total heat flux and NAO. J. Geophys. Res.: Ocean. 115 (C6), http://dx.doi.org/10.1029/2009JC005631, URL: https://agupubs.onlinelibrary.wiley.com/doi/abs/10.1029/2009JC005631, arXiv:https://agupubs.onlinelibrary.wiley.com/doi/pdf/10.1029/2009JC005631.

Pyper, B.J., Peterman, R.M., 1998. Comparison of methods to account for autocorrelation in correlation analyses of fish data. Can. J. Fish. Aquat. Sci. 55 (9), 2127–2140. http://dx.doi.org/10.1139/f98-104, arXiv:10.1139/f98-104.

Raffa, F., Hopkins, T.S., 2004. Circulation and water mass structure over a narrow shelf, augusta gulf (sicily). Chem. Ecol. 20 (sup1), 249–266. http://dx.doi.org/10.1080/02757540410001699857.

Ren, L., Chu, N., Hu, Z., Hartnett, M., 2020. Investigations into synoptic spatiotemporal characteristics of coastal upper ocean circulation using high frequency radar data and model output. Remote. Sens. 12 (17), http://dx.doi.org/10.3390/rs12172841.

Romano, E., Bergamin, L., Croudace, I., Pierfranceschi, G., Sesta, G., Ausili, A., 2021. Measuring anthropogenic impacts on an industrialised coastal marine area using chemical and textural signatures in sediments: A case study of Augusta Harbour (Sicily, Italy). Sci. Total Environ. 755, 142683. http://dx.doi.org/10.1016/j.scitotenv.2020.142683.

Salvagio Manta, D., Bonsignore, M., Oliveri, E., Barra, M., Tranchida, G., Giaramita, L., Mazzola, S., Sprovieri, M., 2016. Fluxes and the mass balance of mercury in Augusta Bay (Sicily, southern Italy). Estuar. Coast. Shelf Sci. 181, 134–143. http://dx.doi.org/10.1016/j.ecss.2016.08.013.

Sprovieri, M., Cucco, A., Budillon, F., Salvagio Manta, D., Trincardi, F., Passaro, S., 2022. Large-scale mercury dispersion at sea: Modelling a multi-hazard case study from Augusta Bay (Central Mediterranean Sea). Int. J. Environ. Res. Public Health 19 (7), http://dx.doi.org/10.3390/ijerph19073956, URL: https://www.mdpi.com/1660-4601/19/7/3956.

Tolkova, E., Power, W., 2011. Obtaining natural oscillatory modes of bays and harbors via empirical orthogonal function analysis of tsunami wave fields. Ocean. Dyn. 61, 731–751. http://dx.doi.org/10.1007/s10236-011-0388-5.

Umgiesser, G., Canu, D., Cucco, A., Solidoro, C., 2004. A finite element model for the venice lagoon. Development, set up, calibration and validation. J. Mar. Syst. 51, 123–145. http://dx.doi.org/10.1016/j.jmarsys.2004.05.009.

Verri, G., Barletta, I., Pinardi, N., Federico, I., Alessandri, J., Coppini, G., 2023. Shelf slope, estuarine dynamics and river plumes in a z* vertical coordinate, unstructured grid model. Ocean. Model. 184, 102235. http://dx.doi.org/10.1016/j.ocemod.2023.102235, URL: https://www.sciencedirect.com/science/article/pii/S1463500323000768.

Zhang, Z., Moore, J.C., 2015. Chapter 6 - empirical orthogonal functions. In: Zhang, Z., Moore, J.C. (Eds.), Mathematical and Physical Fundamentals of Climate Change. Elsevier, Boston, pp. 161–197. http://dx.doi.org/10.1016/B978-0-12-800066-3.00006-1, URL: https://www.sciencedirect.com/science/article/pii/B9780128000663000061.